Available on CMS information server

CMS NOTE 2006/039

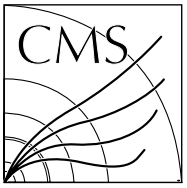

The Compact Muon Solenoid Experiment

CMS Note

Mailing address: CMS CERN, CH-1211 GENEVA 23, Switzerland

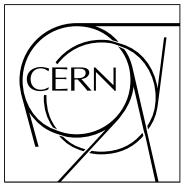

27 January 2006

On the use of $Z \to e^+e^-$ events for ECAL calibration

P. Meridiani, R. Paramatti

INFN - Roma1 and CERN

Abstract

The Z mass constraint in $Z \to e^+e^-$ events is a powerful tool to inter-calibrate ECAL regions, set the absolute energy scale and, ultimately, tune electron reconstruction algorithms. In this note a strategy to use Z events is proposed and tested with a sample of fully simulated $Z \to e^+e^-$ events; the method avoids the inversion of huge matrices. Calibration results obtained with a sample corresponding to 2 fb^{-1} of integrated luminosity are shown. A detailed study on the usage of different electron classes in Z events for calibration purposes is presented.

1 Introduction

The CMS electromagnetic calorimeter is a homogeneous calorimeter built of 75848 lead tungstate ($PbWO_4$) crystals. As expressed in the ECAL TDR [1], an individual inter-calibration of equal or better than 0.5% is required to achieve the ECAL design goal on the energy resolution and hence fully exploit the ECAL physics potential, the benchmark being represented by the discovery of the Higgs Boson in the $H \to \gamma\gamma$ and $H \to ZZ^{(*)} \to 2e^+2e^-$ channels.

The main source of the variation in the barrel channel-to-channel response is the crystal-to-crystal variation of scintillation light yield, which has an RMS of ≈8%; in the endcap the main effect will be instead due to the VPT channel-to-channel variation of the product of the gain, quantum efficiency and photo-cathode area, with a global RMS of almost 25%. The initial inter-calibration will be provided by laboratory measurements of crystal light yield (precision around 4%) [2], [3], pre-calibration of some supermodules with an electron beam (precision around 0.5%) [3], and the commissioning of the supermodules with cosmic rays (attainable precision around 2-3% with one week of cosmic ray data taking) [4]. This means that the ultimately limit on inter-calibration will be fixed by in-situ procedures.

At the beginning of the CMS operation, a fast inter-calibration tool based on the ϕ symmetry of the released energy in a ring of crystals at a certain pseudo-rapidity η can be used to improve the start-up precision [5]. To obtain a global inter-calibration and get rid of possible systematics in the ring-to-ring inter-calibration, this method needs to be complemented by a calibration tool which is able to relate rings at different η. Once the tracker is functional and aligned, the inter-calibration coefficient can be obtained using the tracker momentum measurement as a reference for isolated electrons, mainly coming from $W \to e\nu$ decays. This method is studied in detail in [6]. Other complementary ways to get the channel-to-channel inter-calibration, based on the mass reconstruction in $\pi^0 \to \gamma\gamma$ and $\eta \to \gamma\gamma$ decays, are now under study. A laser monitoring system will be used to correct for the variations in crystal transparency due to radiation damage and subsequent recovery, these variations being fast compared to the timescale of in-situ calibration with physics events.

However, the ECAL calibration does not only deal with inter-calibration. The energy measurement of an electron or a photon will be obtained from the sum of the crystals identified to belong to an electromagnetic cluster by a clustering algorithm. Different clustering algorithms are used to estimate the energy of different electromagnetic objects, such as a fixed array of 5×5 crystals for unconverted photons, or dynamic clustering algorithms [7] for electrons and converted photons. In particular in the latter case, the ECAL clustering is designed to be able to re-collect the energy spread in the ϕ direction due to bremsstrahlung or conversion, building the so called "superclusters" (cluster-of-clusters).

Corrections, which are different for different clustering algorithms and for electrons and photons, are required to relate the cluster energy to the particle's initial energy in order to take into account effects due to partial containment, incomplete bremsstrahlung energy recollection, energy lost in the material in front of the calorimeter. All these corrections are for the moment obtained from Monte Carlo studies on fully simulated samples; however once the CMS detector is operational they need to be extracted from real data. This will be ultimately the fine-tuning of the calorimeter energy scale for different types of particles.

To correctly define the various calibration factors, the relation used to give the energy measurement of a certain calorimeter object, either an electron or a photon, can be written down as:

$$E_{\mathrm{ele},\gamma}(GeV) = \mathcal{F} \times \mathcal{G}(GeV/ADC) \times \sum_i c_i \times A_i(ADC) = \mathcal{F} \times \sum_i E_i(GeV) \qquad (1)$$

where $\mathcal{F}$ is the correction function depending on the particle hypothesis, the clustering algorithm and the position and momentum of the reconstructed particle, $\mathcal{G}$ is a global ADC/GeV conversion factor, while c_i and A_i are respectively the inter-calibration coefficients and the signal amplitudes expressed in ADC counts, which are summed over the clustered crystals; the energy measured in a single crystal has been identified with $E_i(GeV) = \mathcal{G}(GeV/ADC) \times c_i \times A_i(ADC)$.

The nominal Z mass constraint in $Z \to e^+e^-$ decays can be used as a powerful and flexible tool in several tasks: it can be used for regional inter-calibration, without relying on momentum measurements from the tracker, for example as a complement to the ϕ symmetry algorithms at the startup, to set the absolute scale of the calorimeter but also to tune the electron reconstruction algorithms and find the correction factor $\mathcal{F}$ for the various electron reconstruction algorithms. There are also other possibilities to use the Z decays, for example taking advantage of the two different legs of the Z decay, which can be used to check the relative properties between different types of electrons, and compare the distributions obtained from the data to the Monte Carlo predictions.

A study of the calibration method using fully simulated $Z \rightarrow e^+e^-$ events is presented here. The method is currently limitated to Z decays with both e^+ and e^- in the barrel, but it can be extended to other topologies useful to calibrate the entire ECAL.

2 Sample used in the analysis

The Monte Carlo dataset which has been used in this study is a sample of nearly 2 million events. These events have been generated with `PYTHIA 6.223` [9] using the CTEQ5L Parton Distribution Function, the detector simulation has been performed with `CMSIM 132` [10] and the digitization has been done for the low luminosity LHC scenario (nominal luminosity = $2 \times 10^{33} cm^{-2} s^{-1}$) using `ORCA_7_6_1` [11]. Standard preselection cuts have been applied at the generator level: electrons are required to have $p_T > 5$ GeV and $|\eta| < 2.7$. The PYTHIA cross section for $Z \rightarrow e^+e^-$ production at LHC is 1.6 nb; the generator level preselection efficiency is 50.4%. The sample being used in this analysis hence corresponds to an equivalent integrated luminosity of 2.4 fb $^{-1}$.

The pseudorapidity (η) and energy distributions of electrons produced from the Z decay are shown in figures 1 and 2. The p_T distribution is shown in figure 3.

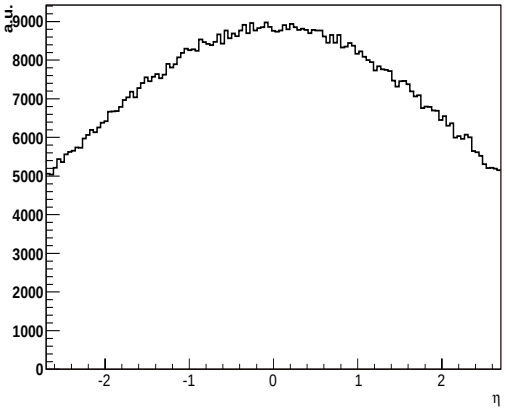

Figure 1: The η distribution at generator level for electrons from $Z \rightarrow e^+e^-$ decays.

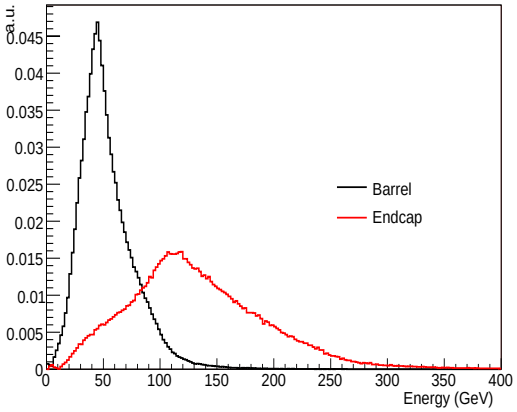

Figure 2: The energy distribution at generator level for electrons from $Z \rightarrow e^+e^-$ decays. Barrel and endcap are separated.

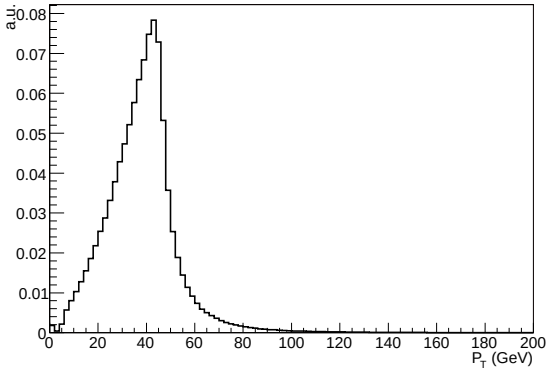

Figure 3: The p_T distribution at generator level for electrons from $Z \rightarrow e^+e^-$ decays. Barrel and endcap are considered together.

Different topologies for the $Z \rightarrow e^+e^-$ decays can be identified: decays where both electrons enter in the ECAL barrel fiducial region ($|\eta| < 1.479$), one electron in the barrel and one in the endcaps ($1.5 < |\eta| < 2.4$), both electrons in the endcaps. Using the PYTHIA cross-section value, the expected rates for the various $Z \rightarrow e^+e^-$

topologies at the nominal LHC low luminosity running conditions, is:

- 0.6 Hz with both electrons in the barrel
- 0.7 Hz with one electron in the barrel and the other one in the endcaps
- 0.3 Hz with both electrons in the endcaps

In this study, only the topology with both electrons in the barrel have been considered. It can be noted, however, that a sufficient number of events will be available to calibrate the endcaps and to relate the endcaps with the barrel.

3 Framework for calibration studies

When dealing with a time consuming task like calibration, computing issues are quite important. Here, millions of events have to be analyzed and many iterations are required on the same events in order to obtain the best estimate of the calibration coefficients. The CMS ORCA framework revealed non optimal to do an analysis like this. For this reason, an efficient data format specifically tuned on calibration requirements has been defined. In this data format, only the information necessary to perform the ECAL calibration starting from electrons are stored in a persistent format different from the ORCA one.

The most important information are the measured energies of the crystals inside a certain region around the electron candidate. Energies of crystals in a matrix of 11 (η) $\times$ 21 (ϕ), centered on the maximum energy crystal, are saved. The window is extending more in the ϕ direction, since the recollection of bremsstrahlung energy is made looking for energy deposits in this direction. When starting from a simulated sample, these are the "perfectly" calibrated energies, which need to be "mis-calibrated" for all the calibration studies. In addition to these quantities, the characteristics of the track associated to the electron candidate (momentum at the vertex and the outermost state, number of tracker hits, χ^2 of the track fit, etc.) and the Monte Carlo truth are the other required information; the event size is around 1 KB per electron. In order to extend the analysis also to the endcap, in the near future also the energy released inside the preshower detector will be included in the persistent data format.

A framework, based on this separate persistent data format, has been developed. This framework allows also to perform complex and flexible tasks, like dynamical clustering, cell navigation, etc. as in the ORCA framework. A flexible energy mis-calibration/calibration mechanism is also present; several possibilities are implemented to generate different starting mis-calibration scenarios.

4 The Z iterative method

The general notation and method is introduced here; however for its generality the Z method can be extended also to other calibration purposes. The main idea is to relate the energy measured in a region j of an event i ($E^{\,i}_{\,j\ meas}$) to the "true" energy (the energy which would have been measured in the region without any mis-calibration): $E^i_{j\ meas} = (1+\varepsilon_j)\cdot E^i_{j\ true}$, where ε_j is zero in the case of a perfectly calibrated region. With this definition, the calibration coefficient of region j would become $c_j = (1+\varepsilon_j)^{-1}$. In this context, the region should be considered in a rather general way and might be either a group of crystals or a single crystal.

The electron energy measurement is the energy sum over the region belonging to the electromagnetic cluster; introducing the weight $w^i_j = E^i_{j\ true}/E^i_{ele\ true}$, one finds:

$$E^i_{ele\ meas} = E^i_{ele\ true}\cdot\left(1+\sum_{j\,\in\,ele}\varepsilon_j w^i_j\right) \tag{2}$$

Assuming θ^i_{12}, the angle between the two electrons in event i, measured by tracks and neglecting the terms $o(\varepsilon^{\,2})$ with respect to $o(\varepsilon)$, the expression for the reconstructed e^+e^- invariant mass is:

$$M^i_{inv} = \sqrt{2\cdot E^i_{ele_1}\cdot E^i_{ele_2}\cdot(1-cos\ \theta^i_{12})} \simeq M_Z\cdot\sqrt{1+\sum_{j\,\in\,ele_1,ele_2}\varepsilon_j w^i_j} \tag{3}$$

where the sum runs over all the regions included in the clusters from both electrons. Each event is related to a linear equation:

$$\left(\frac{M^i_{inv}}{M_Z}\right)^2 - 1 = \sum_j \varepsilon_j w^i_j \tag{4}$$

In order to find the unknown ε_j, one should solve the linear system built with a sample of selected events. However the solution of such a system, where the number of equations is equal to the number of events, is numerically difficult: the presence of two clusters makes the system largely non-diagonal. Furthermore, the weights matrix w_j^i is not known; only its detector estimation is known. Nevertheless, the whole information coming from event i is contained in the ratio M_{inv}^i/M_Z. This is an information not directly related to any particular region, being the single region information folded in an average effect. The problem can be simplified by defining $<\varepsilon>^i$ as the weighted mean of mis-calibration factors in event i (equal to $\sum_j \varepsilon_j w_j^i / \sum_j w_j^i$) and considering that there are two final particles in the event:

$$<\varepsilon>^i = \frac{1}{2} \cdot \left[\left(\frac{M_{inv}^i}{M_Z} \right)^2 - 1 \right] \tag{5}$$

Given a region j, the calibration constant is obtained from the $<\varepsilon>^i$ distribution, where every entry has the weight w_j^i. To reduce the sensitivity to tails, the peak is used to compute the coefficient; this is obtained with an iterative gaussian fit in a region [-2.5σ, 2.5σ] around the peak. A characteristic distribution with the gaussian fit overlaid is shown in figure 4.

Due to the approximations applied in the method, this procedure is iterated until the calibration coefficients converge. After the n^{th} iteration, the calibration constant of region j is the product:

$$C_j = \prod_{iteration}^{n} c_j^k = \prod_{iteration}^{n} \frac{1}{1+\varepsilon_j^k} \tag{6}$$

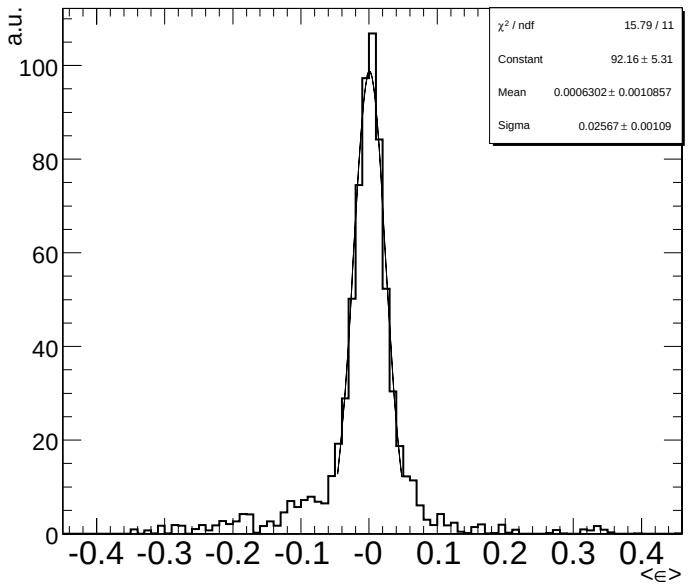

Figure 4: Characteristic distribution of $<\varepsilon>$ with the gaussian fit.

5 Test of the method with a Monte Carlo based selection

A preliminary study has been conducted on the effects of tracker material on the electrons used for the Z mass reconstruction; the aim of this section is to select a class of electrons for which the reconstructed calorimeter energy differs from the initial electron energy only by the non-containment variation (expected to be about 0.7%). A phenomenological approach has been tested, cutting on the fraction of the Bremsstrahlung energy emitted by the electron; this variable is defined as the sum of the photon energy emitted by the electron along its trajectory from the decay vertex to the calorimeter, therefore exploiting the Monte Carlo truth information.

The calorimeter has a modular structure [1]. Modules are of four η types. All the modules are made of 400 crystals (20 in η times 20 in ϕ), except the type 1 module which is made of 500 crystals (25 in η times 20 in ϕ); a "supermodule" is a set of four modules (1700 crystals, 85 in η times 20 in ϕ) and the barrel consists of two identical halves made of 18 supermodules. The Hybrid algorithm [7] is used to reconstruct the electromagnetic clusters; this algorithm uses the η - ϕ geometry of the barrel crystals to exploit the knowledge of the lateral shower shape in the η direction (taking a fixed bar of three or five crystals in η), while searching dynamically for separated (bremsstrahlung) energy in the ϕ direction. The result is the (Hybrid) supercluster.

In figure 5 the distribution of the e^+e^- invariant mass is shown; the only constraint is the presence of at least two electrons in the barrel. Clearly the mean of the distribution is well below the mass of the Z, mainly due to the fact that ECAL superclusters without the energy rescaling (E_{SC}^{raw}) are used and that no cuts on electron Bremsstrahlung are applied.

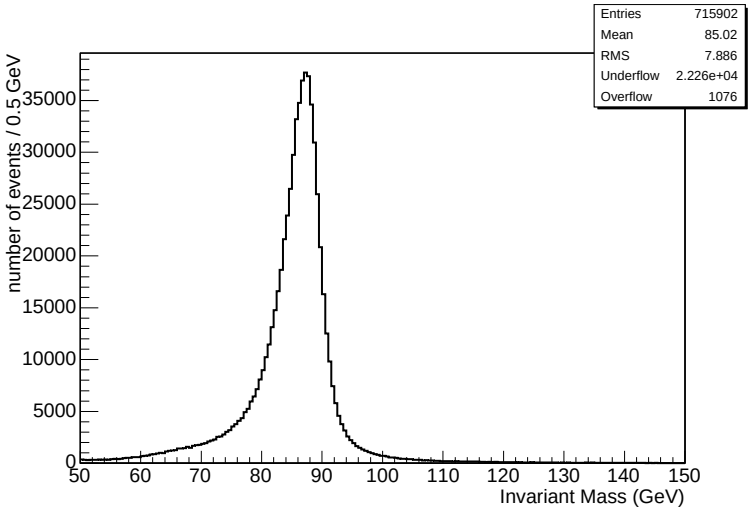

Figure 5: Invariant Mass Distribution of e^+e^- pairs in the barrel. Raw energy of superclusters (E_{SC}^{raw}) are used.

The Z peak position is strongly dependent on the η of both electrons. The dependence of the Z invariant mass on η is shown in figure 6 where the calibration coefficient as a function of the η index of the ring is shown. The calibration coefficient has been computed with the method described in the previous section and corresponds to c_j for each η ring. Here, and in section 7, a calorimeter region is a ring in the ECAL barrel formed by crystals all having the same η value, so that the index j goes from 0 (η = -1.479) to 169 (η = +1.479). Gap effects corresponding to the separations between calorimeter modules and the one in the center (ring index = 84-85) between the two half-barrels are clearly visible. Excluding the module gaps, this dependence is fitted with an even polynomial function, and from the fit function the minimum at η = 0 and the maximum at $|\eta|$ = 1.479 are taken.

No Bremsstrahlung cut has been applied at this point; the same procedure is repeated with the addition of the cut $E_{brem} < 10\%, 20\%, ...\ 90\%$ of electron energy on both electrons. The number of selected events and the efficiency goes down very rapidly as shown in figure 7. When the eta-dependence is fitted again, a significant reduction of the difference above is expected; nevertheless, even cutting very hard on the Bremsstrahlung emission, a substantial η effect remains. This is shown in figure 8, where the maximum and the minimum of the fit are reported as a function of E_{brem} cut; due to the amount of tracker material in the region $1 < |\eta| < 1.479$ (figure 12) and hence to the very low efficiency in this region, the statistical errors of the maximum, when cutting on the bremsstrahlung, are much bigger than the statistical errors of the minimum.

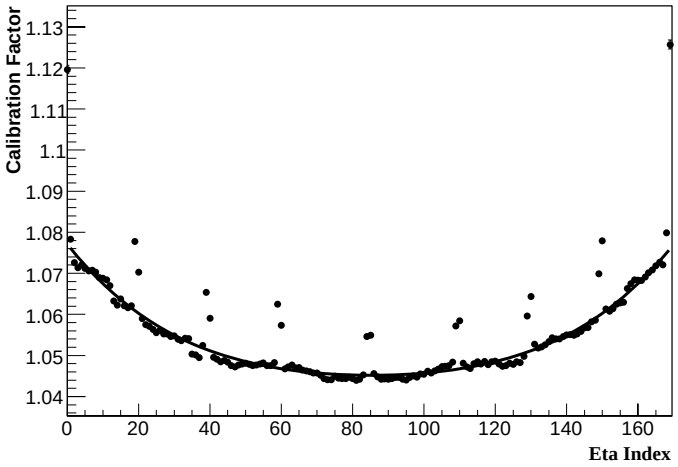

Figure 6: Rescaling factor as a function of barrel ring index.

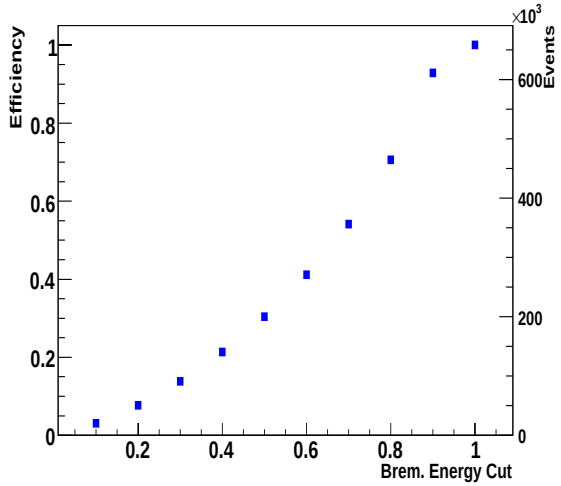

Figure 7: Efficiency of the $Z \rightarrow e^+e^-$ selection as a function of the E_{brem} cut (the statistical error is always below 0.0006, not visible in the plot). The cut is applied to both electrons.

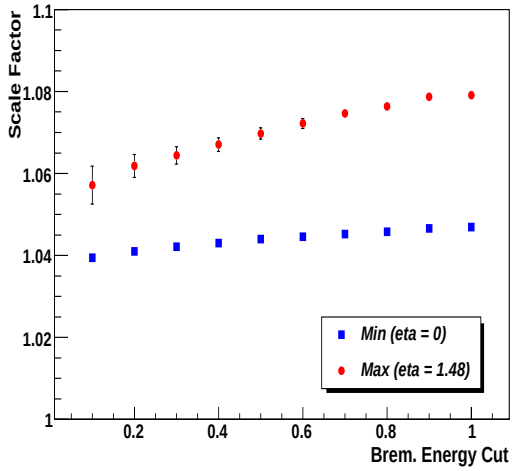

Figure 8: Minimum and maximum of calibration factors (as in figure 6) as a function of the E_{brem} cut.

6 Electron reconstruction and selection

In the previous section it has been shown that even cutting very hard on the true bremsstrahlung energy emitted by the electron, it is not possible to obtain a uniformity in the Z mass reconstruction compatible only with the variation in η of the non-containment. Nevertheless, a selection capable of identifying the electrons, for which the material effects are minimized, is mandatory. It is in fact dangerous to use, for inter-calibration purposes, the whole electron sample since systematic biases, due the limited knowledge of the material in front of the calorimeter, can be very large.

An electron classification based on the different track-cluster associations, as described in [8], has been found useful to accomplish this task. The electron candidate is built by matching a cluster, reconstructed with the Hybrid algorithm, to a track obtained from the Gaussian Sum Filter (GSF) algorithm [8]. The main difference with respect to the HLT electron candidate reconstruction [12] is in the tracking algorithm, which uses a GSF track fitting/smoothing algorithm instead of a simple Kalman Filter, giving the possibility of a better description of the effective electron energy loss distribution in the tracker material.

Four electron classes (*Golden*, *Narrow*, *Big Brem* and *Showering*) are defined. The first class includes high-quality electrons with no evidence of accompanying bremsstrahlung. Electrons compatible with significant radiation are instead assigned to the other classes, following increasing evidence for bremsstrahlung. The *Showering* class, in particular, includes all electrons with identified bremsstrahlung subclusters. A fifth class (*Crack*) comprises electrons falling in regions close to module borders; these electrons require a special treatment and are not used in the present analysis. Electrons having $|\eta|$ greater than 1.444 are also not considered.

In figure 9 the selection efficiency of the different classes of electrons, from $Z \rightarrow e^+e^-$ decays, is shown as a function of the fraction of radiated energy, as measured with Monte Carlo truth information. More than 50% of the electrons which have radiated less than 10% of their energy are identified as *golden* electrons, while more than 70% of the electrons which have radiated more than 90% of their initial energy are classified as *showering*. Electrons radiating a big fraction of their energy only in the last part of the tracker (near ECAL) can still belong to the *golden* class; in fact these electrons fill up the tail of the *golden* class in figure 9. In figure 10, the normalized distributions of the radiated energy for the various classes is shown. It is evident, from this figure, that the *golden* electron class is able to select electrons with a small amount of radiation, which are the electrons that are less affected by the tracker material.

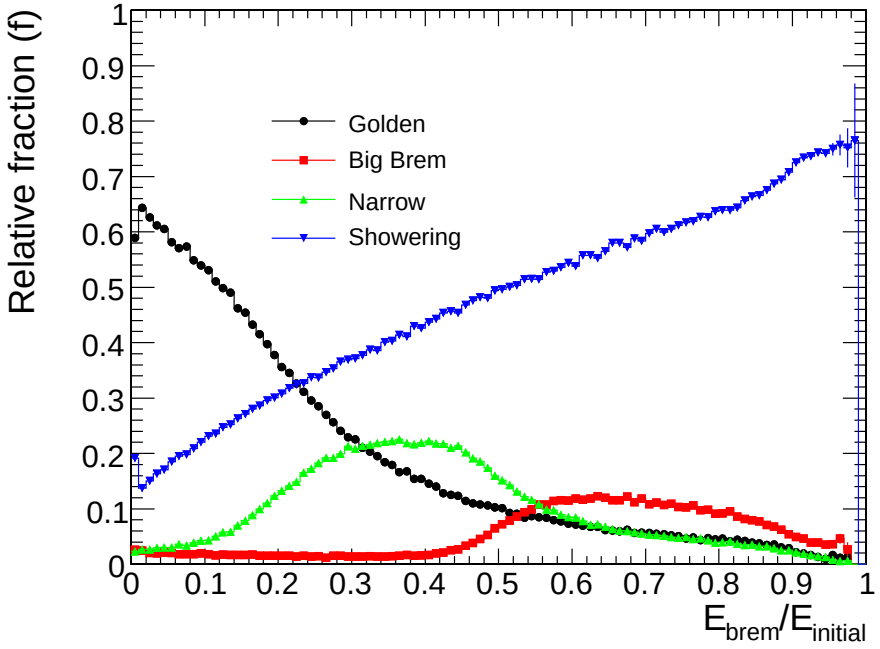

Figure 9: The fraction f of the different electron classes as a function of $E_{brem}/E_{initial}$ (defined with MC-truth information).

The fraction of identified electrons of different classes with respect to the reconstructed electrons changes with the distribution of the tracker material, that is with the η coordinate. In figure 11 this fraction is shown for electrons

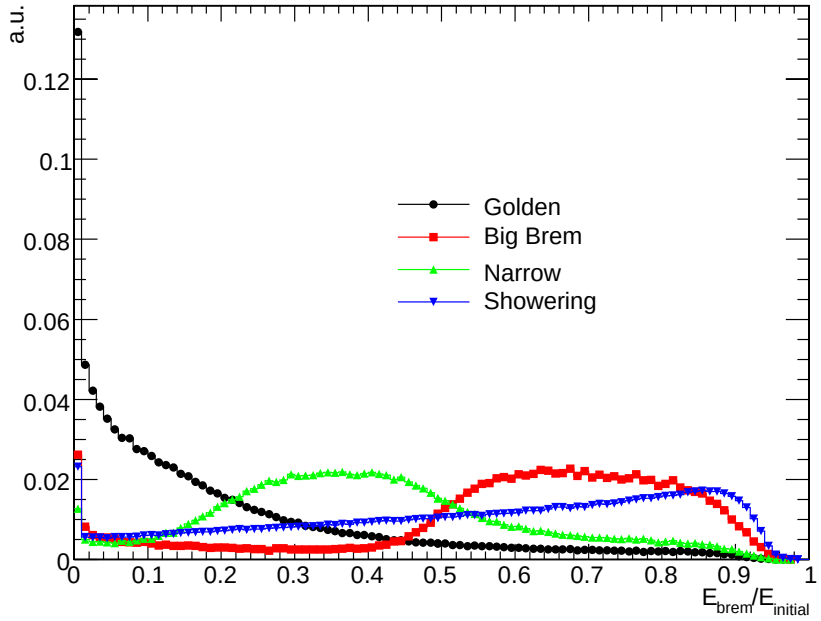

Figure 10: Normalized distributions of $E_{brem}/E_{initial}$ (defined with MC-truth information) for different electron classes.

from $Z \to e^+e^-$ decays as a function of η. In the first calorimeter module ($|\eta| < 0.438$) on average about 40% of these electrons are identified as *golden*, hence hardly radiating or not radiating, while this fraction decreases to less than 10% for the last ECAL barrel module ($1.136 < |\eta| < 1.479$). In this last module more than 70% of the electrons are classified as *showering*.

The variation of the fractions follows the distribution of the material in front of the calorimeter (figure 12), which goes from $\sim 0.5\ X_0$ on average for the region occupied by the first calorimeter module, to around $1.2\ X_0$ for the last calorimeter module.

The global efficiency in the barrel for single electrons from $Z \to e^+e^-$ decays is reported for each class in table 1. The Z decays with both legs identified as *golden* are selected with an efficiency of 5.6%.

Table 1: Efficiency (ε), defined with respect to reconstructed electrons, to select one electron from the $Z \to e^+e^-$ decay in the barrel belonging to the different electron classes

Class	ε
Golden	23.5%
Big Brem	5.2%
Narrow	9.6%
Showering	43.5%
Cracks	18.2%

The invariant mass distributions for e^+e^- pairs from the Z decays, calculated using the energy E_{SC}^{raw}, are shown in figure 13; for each distributions both electrons are required to belong to the same class.

The uniformity of the reconstruction as a function of η for each class is of great interest for regional inter-calibration purposes. To present this effect, the mean of E_{SC}^{raw} divided by the initial electron energy E_{true} as function of η can be visualized for each electron class, as it is shown in figure 14. Electrons belonging to the *golden* electron class show the best uniformity of reconstruction over η, with a variation of the mean of the distribution of about 2% from the start to the end of the barrel. This number increases to 6% for *showering electrons*.

The non-uniformity of the reconstructed energy over η is very similar for *golden*, *big brem* and *narrow* electrons. This means that the impact of the radiated energy, which has very different distributions, is minimal. It is reasonable to assume that *golden* electrons are those with minimal impact from the tracker material. However, they show a

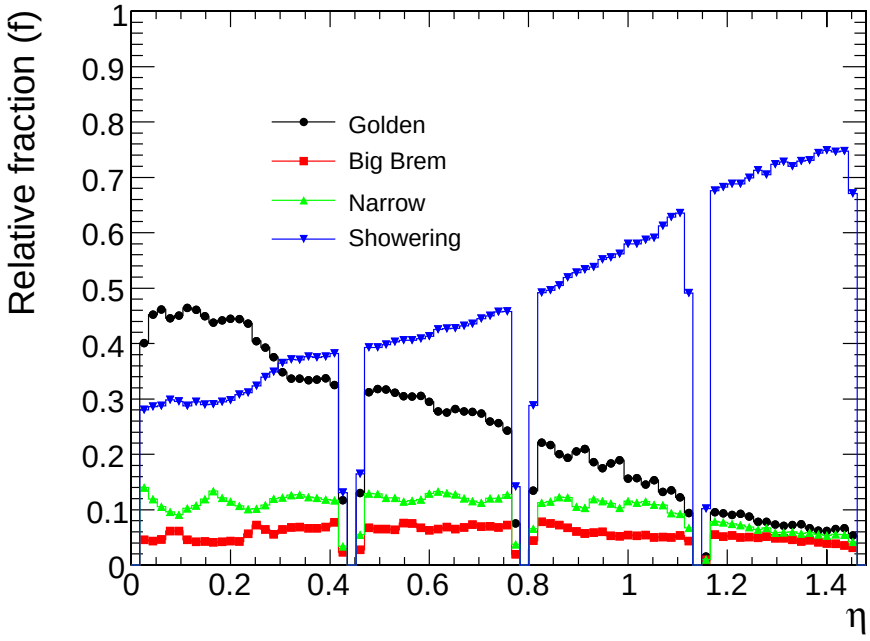

Figure 11: Fraction f of electrons in each class as a function of η.

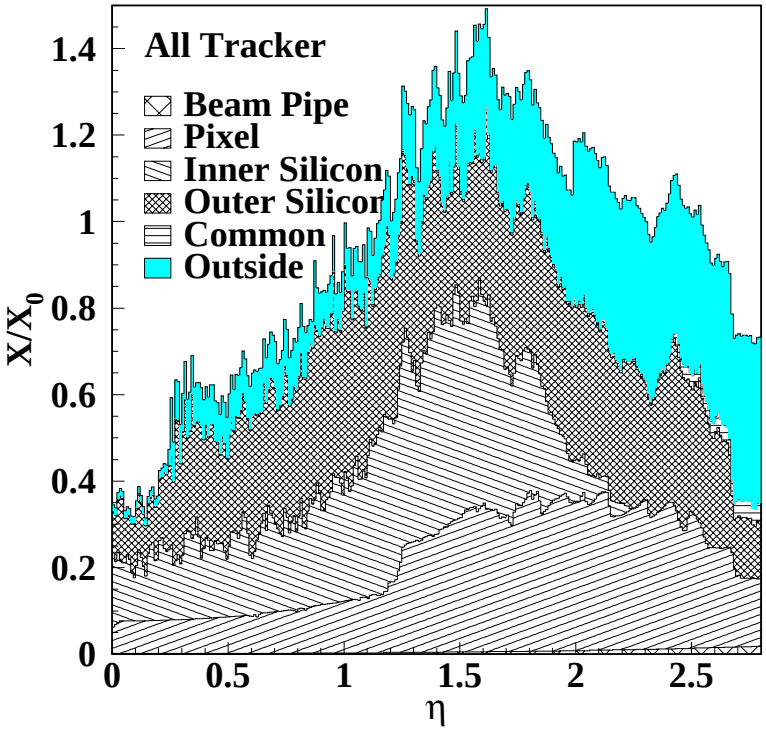

Figure 12: Tracker material budget in terms of radiation length X_0.

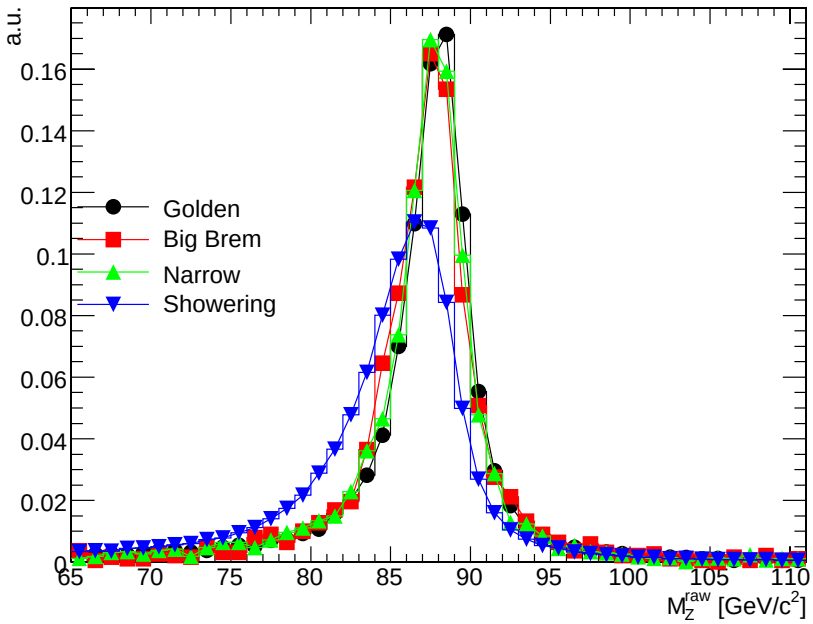

Figure 13: Invariant mass reconstructed with E_{SC}^{raw} when requiring both electrons to belong to the same class. All distributions are normalized to unity.

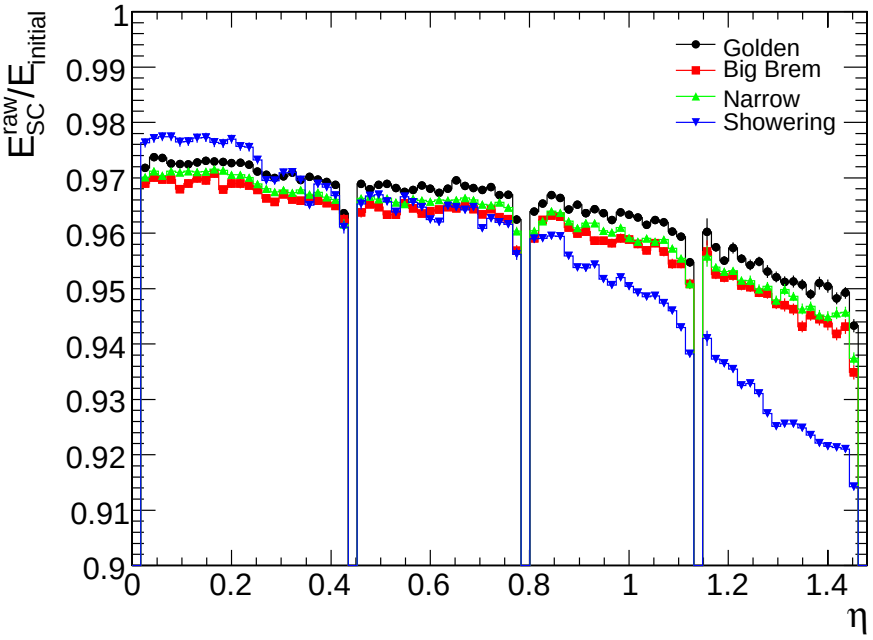

Figure 14: Average of E_{SC}^{raw} divided by E_{true} as function of η for each electron class

variation of 2% over η, which needs to be corrected for in order to be used for inter-calibration purposes. This is the coefficient $\mathcal{F}$ in relation (1), which needs to be factorized away when aiming to obtain the global inter-calibration factors. In particular, the coefficient $\mathcal{F}$ can be written as the product of two terms:

$$\mathcal{F} = \mathcal{F}(N_{cry}) \times \mathcal{F}(\eta). \tag{7}$$

where $\mathcal{F}(N_{cry})$ depend on the number of crystals in the seed cluster (the cluster having the highest fraction of energy) of the supercluster, and $\mathcal{F}(\eta)$ depend on η. The same $\mathcal{F}(N_{cry})$ is used for all electron classes, but two different $\mathcal{F}(\eta)$ are needed, one for *showering* electrons and one for all other classes, since impact of material is quite important for the *showering* class, as discussed earlier. The distribution of the Z invariant mass, calculated with the corrected supercluster energy, is shown in figure 15, where both electrons are required to belong to the same class and the energy corrections as described in [8] are applied. The correction for the *showering* class does not seem to be perfectly tuned for electrons from Z decays and should be improved.

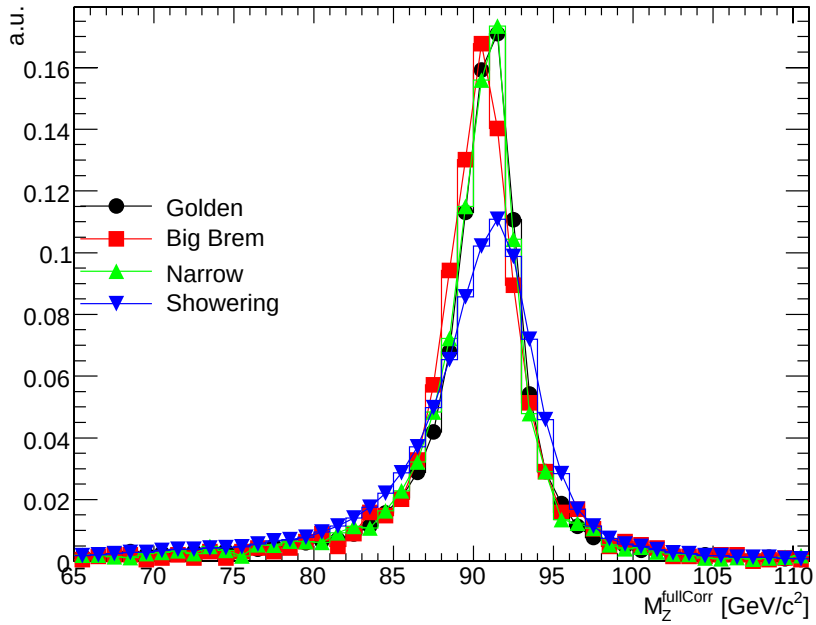

Figure 15: The e^+e^- invariant mass from Z decays, calculated with corrected supercluster energy, requiring both electrons to belong to the same class. All distributions are normalized to unity.

7 Inter-calibration of crystal rings to be applied following the ϕ-symmetry approach

A fast inter-calibration method based on the physics and detector ϕ-symmetry is foreseen at the LHC start-up [5]; the goal of this method is to inter-calibrate crystals belonging to an η slice of the calorimeter. In this section, the Z method is used to inter-calibrate the barrel rings. Only Z's with both legs being *golden* electrons are selected. Corrections to the reconstructed energy described in the previous section are applied. Rings with crystals belonging to the module borders are not considered.

The Z inter-calibration has been performed with different mis-calibration values between crystals inside the ring (0%, 2% and 5%) and between different rings (0%, 5% and 10%). Stable results have been obtained for all of them. The capability of the Z method is tested by comparing the artificial mis-calibration (m_j) with respect to the calibration coefficient (c_j) of the same channel; the residual used to measure the resolution is defined as $\delta = (m \cdot c - 1)$. Starting with a 5% mis-calibration between the rings and 2% inside each ring, the distribution of the residual as a function of the η index, shown in figure 16, is obtained with a sample of events equivalent to an integrated luminosity of 2 fb^{-1}. The HLT efficiency, which is close to one for $Z \to e^+e^-$ events with both *golden* electrons, is not accounted for. The achievable ring inter-calibration precision with this amount of data, i.e. the spread of the residual distribution (σ_{cal}), is 0.6% as shown in figure 17. The ring inter-calibration precisions per module types are summarized in table 2.

Table 2: The inter-calibration precision (σ_{cal}) with a sample equivalent to an integrated luminosity of 2 fb^{-1}.

Module Type	σ_{cal}
1	$0.46\% \pm 0.05\%$
2	$0.5\% \pm 0.1\%$
3	$0.6\% \pm 0.1\%$
4	$1.0\% \pm 0.1\%$

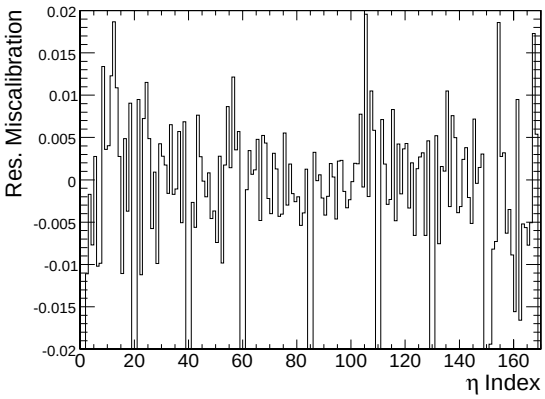

Figure 16: Residual mis-calibration (δ) versus the η index.

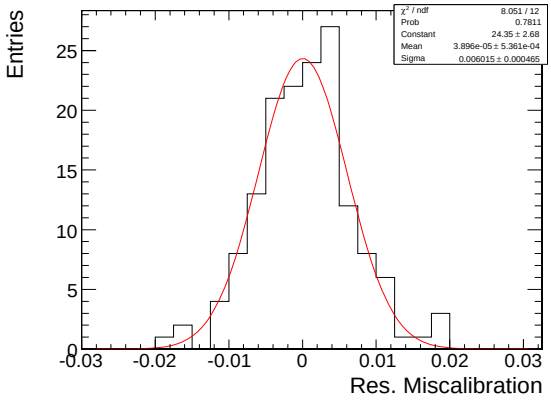

Figure 17: Distribution of δ with a sample equivalent to an integrated luminosity of 2 fb^{-1}.

The calibration precision as a function of the event statistics per ring is shown in figure 18; the event statistics is defined as the mean of $\sum_{event\ i} w_j^i$. The point corresponding to 2.0 fb^{-1} is the second last, with an average of 365 events per ring. No systematic effects are observed as a function of the module type (figure 19).

The asymptotic precision does not depend on the initial spread of the mis-calibration values; the number of selected events as a function of the iteration is shown in figure 20 (left) where mis-calibrations of respectively 0%, 2% and 5% are applied between the crystals of the same ring. The event selection is repeated after each iteration; hence, even if the number of selected events at the beginning is different, the calibrations converge to the same set of events. The inter-calibration precision versus the iteration is shown in figure 20 (right). These plots correspond to an integrated luminosity of 2.0 fb^{-1}.

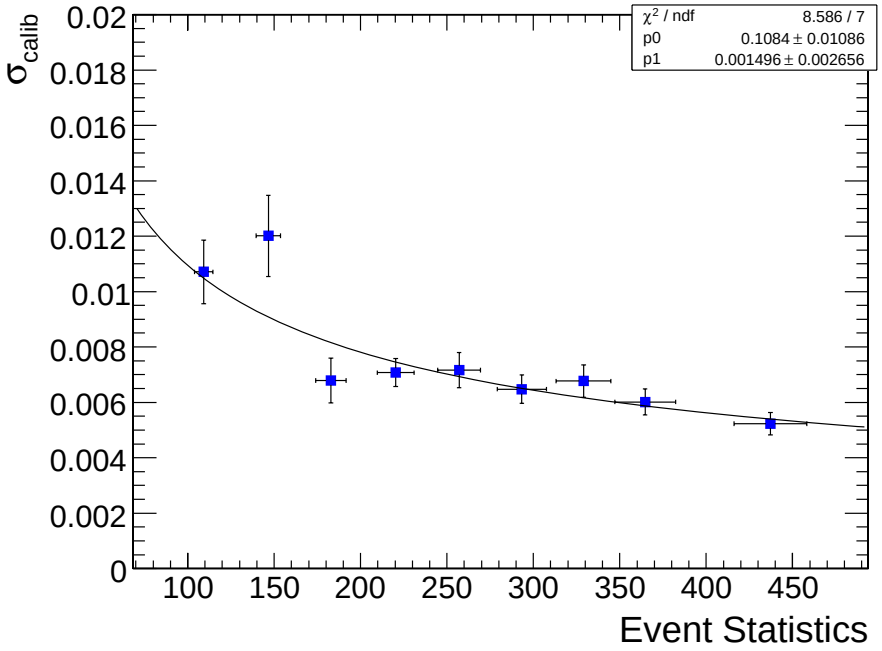

Figure 18: Ring inter-calibration precision as a function of the event statistics; the event statistics is defined as the average of $\sum_{event\ i} w_j^i$ on the ring. A fit to the function $p1 + p0/\sqrt{N}$ is superimposed. The point corresponding to 2.0 fb^{-1} is the one before the last.

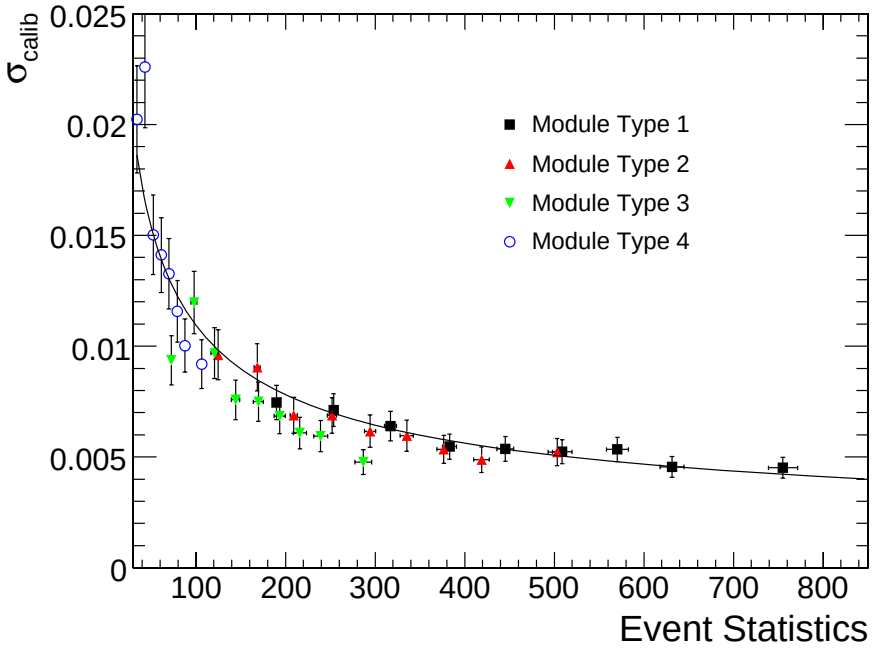

Figure 19: Ring inter-calibration precision for different module type as a function of the event statistics; the event statistics is defined as the mean of $\sum_{event\ i} w_j^i$. The function obtained in figure 18 is superimposed.

8 Use of $Z \to e^+e^-$ events to tune electron reconstruction algorithms

A complementary and different use of $Z \to e^+e^-$ events can be the tuning of the factor $\mathcal{F}$, the rescaling needed to relate the energy contained in the calorimeter cluster to the initial electron energy, in order to take into account shower non-containment and material effects. However, this means that in order to use $Z \to e^+e^-$ events for this purpose a preliminary global inter-calibration by different physics channels is needed.

Fed with a global-inter-calibration, the algorithm described in section 4 is able to find the $\mathcal{F}(\eta)$ corrections, as

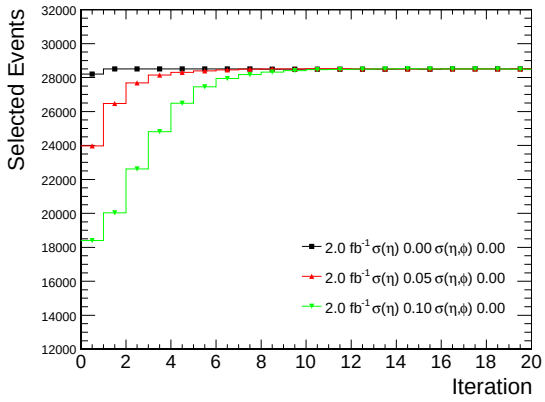

(a) No mis-calibration inside each ring

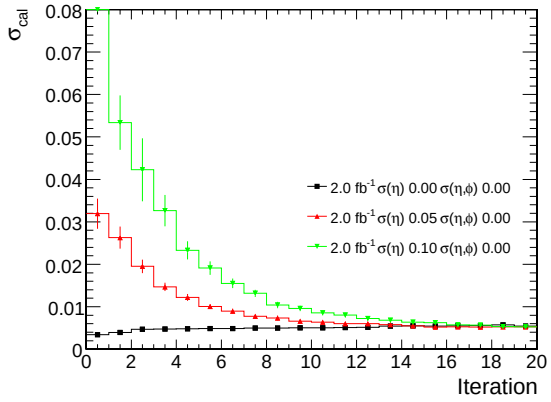

(b) No mis-calibration inside each ring

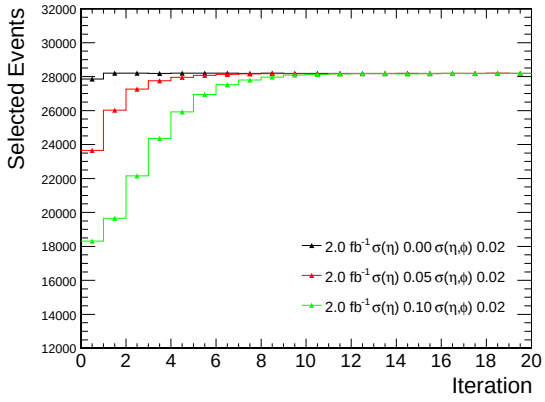

(c) Mis-calibration of 2% inside each ring

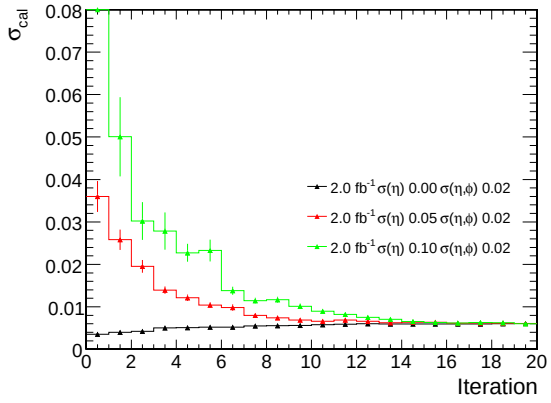

(d) Mis-calibration of 2% inside each ring

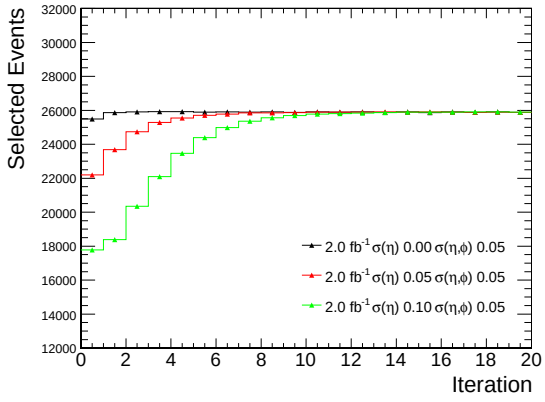

(e) Mis-calibration of 5% inside each ring

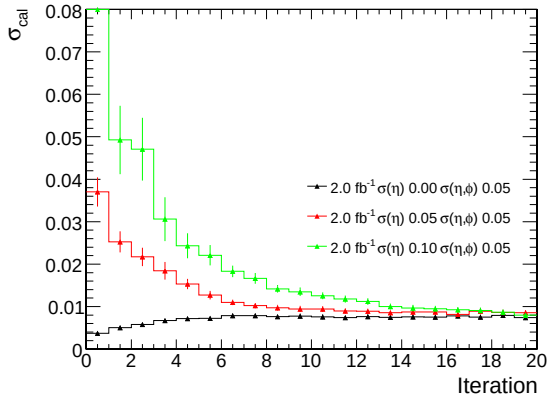

(f) Mis-calibration of 5% inside each ring

Figure 20: (a), (c), (e): number of selected events versus iteration. (b), (d), (f): inter-calibration precision versus iteration. The mis-calibration between different rings is 0%, 5% and 10%, the equivalent integrated luminosity is 2 fb^{-1}.

defined in equation 7, which are different for the various electron classes; one is needed for the *showering* electrons, and one for the remaining classes.

In order to test the capability of the algorithm, the method has been tested with a global mis-calibration of 2% between barrel crystals. Z events have been selected in two ways:

- both electrons belonging to the *golden* class
- both electrons belonging to the *showering* class

The electron energy used to compute the invariant mass is here corrected only using the $\mathcal{F}(N_{cry})$ function defined in equation 7.

The results of the test with a sample corresponding to an integrated luminosity of 2 fb $^{-1}$ is presented in figure 21. The shape of the functions, which are the $\mathcal{F}(\eta)$ corrections for *golden* and for *showering* electrons as tuned in [8], seems to be very well reproduced by the points, which are obtained from the mean of the rescaling coefficient in different η regions. A global rescaling factor (1.0045 $\pm$ 0.0004 for *golden* and 1.0082 $\pm$ 0.0004 for *showering* electrons) is applied to $\mathcal{F}(\eta)$ in order to get a better agreement. This factor is due to the different electron energies in the Z sample with respect to the electrons used in [8].

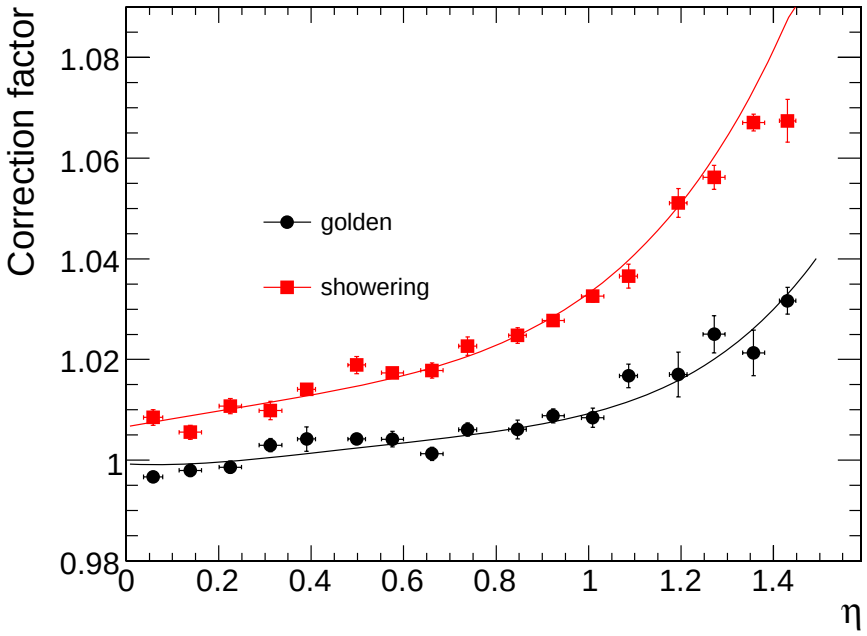

Figure 21: Correction factors versus η; points are the average of the rescaling coefficients in the η region, the line is the function $\mathcal{F}(\eta)$ as explained in the text.

From the two plots 22 and 23, showing the normalized residuals between the points and the reference function of figure 21 for the *golden* and *showering* class respectively, it can be seen that no evident bias is present. In conclusion, the $Z \rightarrow e^+e^-$ events can be effectively used as a powerful tool to tune the electron energy reconstruction algorithms.

9 Use of Z events to measure the absolute energy scale

The absolute energy scale of the calorimeter can also be obtained with $Z \rightarrow e^+e^-$ events. In section 7 the spread of the m_j was fixed to different values, the average being always one. Within the calibration framework it is possible to change the average mis-calibration as well, able to simulate an absolute energy scale different from unity in the calorimeter. The calibration procedure must be capable to recover this injected scale factor without any bias.

This test has been performed by applying scale factors from -8% to +6% with a 2% step size and using, like in section 7, only *golden* electrons with an equivalent luminosity of 2 fb $^{-1}$. In figure 24 the obtained scale factor, that

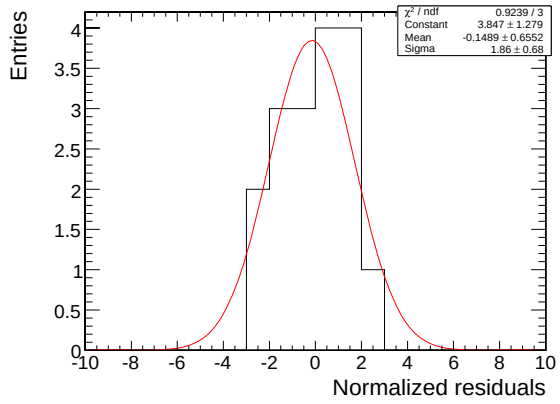

Figure 22: Normalized residuals (pulls) between the points and the function $\mathcal{F}(\eta)$ for the *golden* electrons; no uncertainties are associated to the function.

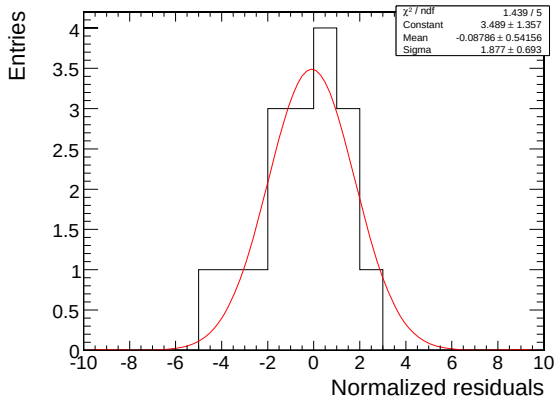

Figure 23: Normalized residuals (pulls) between the points and the function $\mathcal{F}(\eta)$ for the *showering* electrons; no uncertainties are associated to the function.

is the average of the calibration coefficients times the average of the m_j, is shown versus the injected scale factor. No bias is observed with respect to the injected scale.

Furthermore, figure 24 shows that the statistical uncertainty on the energy scale determination using 2 fb $^{-1}$ is about 0.05%.

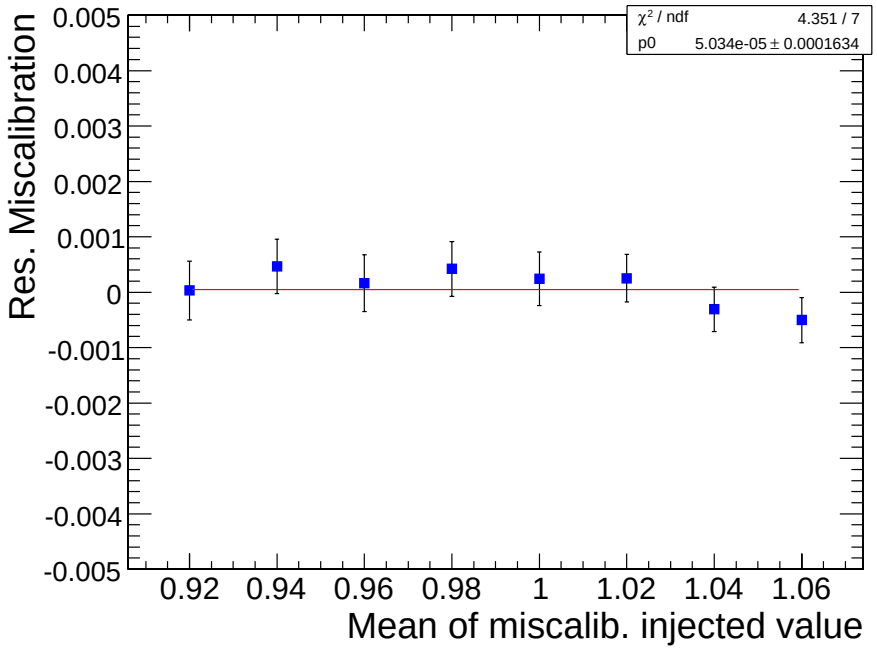

Figure 24: Mean of the residual mis-calibration versus the mean value of the artificial mis-calibrations. A fit with a constant function is superimposed.

10 Conclusions

In this note several aspects of the ECAL calibration with $Z \to e^+e^-$ have been considered. A new iterative method has been described; the performed tests give stable results showing the capability of the method to converge after a few iteration to a set of calibration coefficients independent of the initial crystal energy mis-calibration. Selecting Z events with two *golden* electrons, a barrel ring inter-calibration precision of 0.6% can be obtained with an integrated luminosity of 2 fb^{-1}; the obtained precision varies from 0.45% in the type 1 module region up to 1.0% in the type

4 module region. This difference is mainly due to the change of efficiency in the *golden* electron selection versus η.

Moreover it has been proven that electron reconstruction algorithms can be tuned with $Z \to e^+e^-$ events, provided a preliminary ECAL inter-calibration is performed by different physics channels.

Finally the Z iterative method has been tested with a variation of the global mis-calibration scale from -8% to +6%. The method achieves a statistical precision of around 0.05% using the events corresponding to an integrated luminosity of 2 fb^{-1}.

Systematic studies concerning the calibration precision dependence on the electron selection criteria are foreseen; for example, the combination of different electron classes can be used. In particular, the effects due to the variation of the tracker material distribution need to be extensively studied. This will also reinforce the robustness of the method in order to use it at the beginning of the LHC operations, where probably an extensive knowledge of the material in front of the calorimeter will not be available. An extension of the method for the endcap and barrel-endcap inter-calibration is also foreseen.

11 Acknowledgments

We would like to gratefully thank the entire CMS ECAL e/γ community for having supported this work from the beginning. In particular we are indebted to the people of the CMS ECAL groups of LLR - Ecole Polytechnique (S. Baffioni, C. Charlot, Y. Sirois), Milano Bicocca (F. Ferri, C. Rovelli, P. Govoni, M. Paganoni, R. Salerno) and FESB - Split (I. Puljak), for the cooperation and rapid feed-back in the electron reconstruction studies. A special thank goes also to L. Malgeri and C. Seez for their precious guidance throughout all the work and to W. Adam, G. Dissertori, S. Rahatlou, R. Tenchini and R.Y. Zhu for their useful comments.

References

[1] CMS Collaboration, *"The CMS Electromagnetic Calorimeter Technical Design Report"*, CERN/LHCC 97-33

[2] F. Cavallari et al., *"Relative Light Yield comparison between laboratory and testbeam data for CMS ECAL $PbWO_4$ crystals"*, CMS Rapid Note 2004/002

[3] The CMS Electromagnetic Calorimeter Group, *"Results of the first performance tests of the CMS electromagnetic calorimeter"*, The European Physical Journal C - Particles and Fields, Volume 44, Jan 2006, Pages 1 - 10

[4] W. Bertl et al, *"Feasibility of Intercalibration of CMS ECAL Supermodules with Cosmic Rays"*, CMS Note 2004/036
M. Bonesini et al, *"Inter-calibration of the CMS electromagnetic calorimeter with cosmic rays before installation"*, CMS Note 2005/023

[5] D. Futyan, C. Seez, *"Intercalibration of ECAL crystals in ϕ Using Symmetry of Energy Deposition"*, CMS Note 2002/031
D. Futyan, *"Intercalibration of the CMS Electromagnetic Calorimeter Using Jet Trigger Events"*, CMS Note 2004/007

[6] G. Daskalakis et al., *"Inter-Calibration of the CMS Electromagnetic Calorimeter with Isolated Electrons"*, CMS Note 2006/021

[7] E. Meschi et al., *"Electron reconstruction in the CMS Electromagnetic Calorimeter"*, CMS Note 2001/034

[8] S. Baffioni et al., *"Electron reconstruction in CMS"*, CMS Note 2006/040

[9] T. Sjostrand, L. Lonnblad, and S. Mrenna, *"PYTHIA 6.2: Physics and manual"*, arXiv:hep-ph/0108264.

[10] *"CMSIM: CMS Simulation Package"* (obsolete), available at http://cmsdoc.cern.ch/cmsim/cmsim.html

[11] *"ORCA: CMS Reconstruction Package"*, site located at http://cmsdoc.cern.ch/orca

[12] CMS Collaboration, *"Data Acquisition & High-Level Trigger Technical Design Report"*, CERN/LHCC 2002-26